

# A Measurement of the Hadronic Decay Current and the $\nu_\tau$ -helicity in $\tau^- \rightarrow \pi^- \pi^- \pi^+ \nu_\tau$

## The OPAL Collaboration

### Abstract

The decay  $\tau^- \rightarrow \pi^- \pi^- \pi^+ \nu_\tau$  has been studied using data collected with the OPAL detector at LEP during 1992 to 1994. Models of Kühn and Santamaria and of Isgur et al. are used to fit distributions of the  $3\pi$  invariant mass squared as well as  $2\pi$  invariant mass squared projections of the Dalitz plot, and the model dependent mass and width of the  $a_1$  resonance are measured for both models. Neither model, however, is found to provide a completely satisfactory description of the data. The hadronic structure functions for this decay are measured in a model independent framework. No evidence for vector or scalar currents has been found. In addition, the parity violating asymmetry parameter is measured in a model independent way to be  $\gamma_{VA} = 1.29 \pm 0.26 \pm 0.11$ .

(Submitted to Zeit. f. Physik C)

# The OPAL Collaboration

K. Ackerstaff<sup>8</sup>, G. Alexander<sup>23</sup>, J. Allison<sup>16</sup>, N. Altekamp<sup>5</sup>, K. Ametewee<sup>25</sup>, K.J. Anderson<sup>9</sup>, S. Anderson<sup>12</sup>, S. Arceci<sup>2</sup>, S. Asai<sup>24</sup>, D. Axen<sup>29</sup>, G. Azuelos<sup>18,a</sup>, A.H. Ball<sup>17</sup>, E. Barberio<sup>8</sup>, R.J. Barlow<sup>16</sup>, R. Bartoldus<sup>3</sup>, J.R. Batley<sup>5</sup>, J. Bechtluft<sup>14</sup>, C. Beeston<sup>16</sup>, T. Behnke<sup>8</sup>, A.N. Bell<sup>1</sup>, K.W. Bell<sup>20</sup>, G. Bella<sup>23</sup>, S. Bentvelsen<sup>8</sup>, P. Berlich<sup>10</sup>, S. Bethke<sup>14</sup>, O. Biebel<sup>14</sup>, A. Biguzzi<sup>5</sup>, S.D. Bird<sup>16</sup>, V. Blobel<sup>27</sup>, I.J. Bloodworth<sup>1</sup>, J.E. Bloomer<sup>1</sup>, M. Bobinski<sup>10</sup>, P. Bock<sup>11</sup>, H.M. Bosch<sup>11</sup>, M. Boutemur<sup>34</sup>, B.T. Bouwens<sup>12</sup>, S. Braibant<sup>12</sup>, R.M. Brown<sup>20</sup>, H.J. Burckhart<sup>8</sup>, C. Burgard<sup>8</sup>, R. Bürgin<sup>10</sup>, P. Capiluppi<sup>2</sup>, R.K. Carnegie<sup>6</sup>, A.A. Carter<sup>13</sup>, J.R. Carter<sup>5</sup>, C.Y. Chang<sup>17</sup>, D.G. Charlton<sup>1,b</sup>, D. Chrisman<sup>4</sup>, P.E.L. Clarke<sup>15</sup>, I. Cohen<sup>23</sup>, J.E. Conboy<sup>15</sup>, O.C. Cooke<sup>16</sup>, M. Cuffiani<sup>2</sup>, S. Dado<sup>22</sup>, C. Dallapiccola<sup>17</sup>, G.M. Dallavalle<sup>2</sup>, S. De Jong<sup>12</sup>, L.A. del Pozo<sup>4</sup>, K. Desch<sup>3</sup>, M.S. Dixit<sup>7</sup>, E. do Couto e Silva<sup>12</sup>, M. Doucet<sup>18</sup>, E. Duchovni<sup>26</sup>, G. Duckeck<sup>34</sup>, I.P. Duerdoth<sup>16</sup>, D. Eatough<sup>16</sup>, J.E.G. Edwards<sup>16</sup>, P.G. Estabrooks<sup>6</sup>, H.G. Evans<sup>9</sup>, M. Evans<sup>13</sup>, F. Fabbrì<sup>2</sup>, M. Fanti<sup>2</sup>, P. Fath<sup>11</sup>, A.A. Faust<sup>30</sup>, F. Fiedler<sup>27</sup>, M. Fierro<sup>2</sup>, H.M. Fischer<sup>3</sup>, R. Folman<sup>26</sup>, D.G. Fong<sup>17</sup>, M. Foucher<sup>17</sup>, A. Fürtes<sup>8</sup>, P. Gagnon<sup>7</sup>, A. Gaidot<sup>21</sup>, J.W. Gary<sup>4</sup>, J. Gascon<sup>18</sup>, S.M. Gascon-Shotkin<sup>17</sup>, N.I. Geddes<sup>20</sup>, C. Geich-Gimbel<sup>3</sup>, F.X. Gentit<sup>21</sup>, T. Geralis<sup>20</sup>, G. Giacomelli<sup>2</sup>, P. Giacomelli<sup>4</sup>, R. Giacomelli<sup>2</sup>, V. Gibson<sup>5</sup>, W.R. Gibson<sup>13</sup>, D.M. Gingrich<sup>30,a</sup>, D. Glenzinski<sup>9</sup>, J. Goldberg<sup>22</sup>, M.J. Goodrick<sup>5</sup>, W. Gorn<sup>4</sup>, C. Grandi<sup>2</sup>, E. Gross<sup>26</sup>, J. Grunhaus<sup>23</sup>, M. Gruwé<sup>8</sup>, C. Hajdu<sup>32</sup>, G.G. Hanson<sup>12</sup>, M. Hansroul<sup>8</sup>, M. Hapke<sup>13</sup>, C.K. Hargrove<sup>7</sup>, P.A. Hart<sup>9</sup>, C. Hartmann<sup>3</sup>, M. Hauschild<sup>8</sup>, C.M. Hawkes<sup>5</sup>, R. Hawkings<sup>27</sup>, R.J. Hemingway<sup>6</sup>, M. Herndon<sup>17</sup>, G. Herten<sup>10</sup>, R.D. Heuer<sup>8</sup>, M.D. Hildreth<sup>8</sup>, J.C. Hill<sup>5</sup>, S.J. Hillier<sup>1</sup>, T. Hilse<sup>10</sup>, P.R. Hobson<sup>25</sup>, R.J. Homer<sup>1</sup>, A.K. Honma<sup>28,a</sup>, D. Horváth<sup>32,c</sup>, R. Howard<sup>29</sup>, R.E. Hughes-Jones<sup>16</sup>, D.E. Hutchcroft<sup>5</sup>, P. Igo-Kemenes<sup>11</sup>, D.C. Imrie<sup>25</sup>, M.R. Ingram<sup>16</sup>, K. Ishii<sup>24</sup>, A. Jawahery<sup>17</sup>, P.W. Jeffreys<sup>20</sup>, H. Jeremie<sup>18</sup>, M. Jimack<sup>1</sup>, A. Joly<sup>18</sup>, C.R. Jones<sup>5</sup>, G. Jones<sup>16</sup>, M. Jones<sup>6</sup>, R.W.L. Jones<sup>8</sup>, U. Jost<sup>11</sup>, P. Jovanovic<sup>1</sup>, T.R. Junk<sup>8</sup>, D. Karlen<sup>6</sup>, K. Kawagoe<sup>24</sup>, T. Kawamoto<sup>24</sup>, R.K. Keeler<sup>28</sup>, R.G. Kellogg<sup>17</sup>, B.W. Kennedy<sup>20</sup>, J. Kirk<sup>29</sup>, S. Kluth<sup>8</sup>, T. Kobayashi<sup>24</sup>, M. Kobel<sup>10</sup>, D.S. Koetke<sup>6</sup>, T.P. Kokott<sup>3</sup>, M. Kolrep<sup>10</sup>, S. Komamiya<sup>24</sup>, T. Kress<sup>11</sup>, P. Krieger<sup>6</sup>, J. von Krogh<sup>11</sup>, P. Kyberd<sup>13</sup>, G.D. Lafferty<sup>16</sup>, H. Lafoux<sup>21</sup>, R. Lahmann<sup>17</sup>, W.P. Lai<sup>19</sup>, D. Lanske<sup>14</sup>, J. Lauber<sup>15</sup>, S.R. Lautenschlager<sup>31</sup>, J.G. Layter<sup>4</sup>, D. Lazic<sup>22</sup>, A.M. Lee<sup>31</sup>, E. Lefebvre<sup>18</sup>, D. Lellouch<sup>26</sup>, J. Letts<sup>12</sup>, L. Levinson<sup>26</sup>, C. Lewis<sup>15</sup>, S.L. Lloyd<sup>13</sup>, F.K. Loebinger<sup>16</sup>, G.D. Long<sup>28</sup>, M.J. Losty<sup>7</sup>, J. Ludwig<sup>10</sup>, A. Macchiolo<sup>2</sup>, A. Macpherson<sup>30</sup>, A. Malik<sup>21</sup>, M. Mannelli<sup>8</sup>, S. Marcellini<sup>2</sup>, C. Markus<sup>3</sup>, A.J. Martin<sup>13</sup>, J.P. Martin<sup>18</sup>, G. Martinez<sup>17</sup>, T. Mashimo<sup>24</sup>, W. Matthews<sup>25</sup>, P. Mättig<sup>3</sup>, W.J. McDonald<sup>30</sup>, J. McKenna<sup>29</sup>, E.A. Mckigney<sup>15</sup>, T.J. McMahon<sup>1</sup>, A.I. McNab<sup>13</sup>, R.A. McPherson<sup>8</sup>, F. Meijers<sup>8</sup>, S. Menke<sup>3</sup>, F.S. Merritt<sup>9</sup>, H. Mes<sup>7</sup>, J. Meyer<sup>27</sup>, A. Michelini<sup>2</sup>, G. Mikenberg<sup>26</sup>, D.J. Miller<sup>15</sup>, R. Mir<sup>26</sup>, W. Mohr<sup>10</sup>, A. Montanari<sup>2</sup>, T. Mori<sup>24</sup>, M. Morii<sup>24</sup>, U. Müller<sup>3</sup>, K. Nagai<sup>26</sup>, I. Nakamura<sup>24</sup>, H.A. Neal<sup>8</sup>, B. Nellen<sup>3</sup>, B. Nijhar<sup>16</sup>, R. Nisius<sup>8</sup>, S.W. O’Neale<sup>1</sup>, F.G. Oakham<sup>7</sup>, F. Odorici<sup>2</sup>, H.O. Ogren<sup>12</sup>, N.J. Oldershaw<sup>16</sup>, T. Omori<sup>24</sup>, M.J. Oreglia<sup>9</sup>, S. Orito<sup>24</sup>, J. Pálinkás<sup>33,d</sup>, G. Pásztor<sup>32</sup>, J.R. Pater<sup>16</sup>, G.N. Patrick<sup>20</sup>, J. Patt<sup>10</sup>, M.J. Pearce<sup>1</sup>, S. Petzold<sup>27</sup>, P. Pfeifenschneider<sup>14</sup>, J.E. Pilcher<sup>9</sup>, J. Pinfold<sup>30</sup>, D.E. Plane<sup>8</sup>, P. Poffenberger<sup>28</sup>, B. Poli<sup>2</sup>, A. Posthaus<sup>3</sup>, H. Przysiezniak<sup>30</sup>, D.L. Rees<sup>1</sup>, D. Rigby<sup>1</sup>, S. Robertson<sup>28</sup>, S.A. Robins<sup>13</sup>, N. Rodning<sup>30</sup>, J.M. Roney<sup>28</sup>, A. Rooke<sup>15</sup>, E. Ros<sup>8</sup>, A.M. Rossi<sup>2</sup>, M. Rosvick<sup>28</sup>, P. Routenburg<sup>30</sup>, Y. Rozen<sup>22</sup>, K. Runge<sup>10</sup>, O. Runolfsson<sup>8</sup>, U. Ruppel<sup>14</sup>, D.R. Rust<sup>12</sup>, R. Rylko<sup>25</sup>, K. Sachs<sup>10</sup>, E.K.G. Sarkisyan<sup>23</sup>, M. Sasaki<sup>24</sup>, C. Sbarra<sup>29</sup>, A.D. Schaile<sup>34</sup>,

O. Schaile<sup>34</sup>, F. Scharf<sup>3</sup>, P. Scharff-Hansen<sup>8</sup>, P. Schenk<sup>34</sup>, B. Schmitt<sup>8</sup>, S. Schmitt<sup>11</sup>,  
M. Schröder<sup>8</sup>, H.C. Schultz-Coulon<sup>10</sup>, M. Schulz<sup>8</sup>, M. Schumacher<sup>3</sup>, P. Schütz<sup>3</sup>, W.G. Scott<sup>20</sup>,  
T.G. Shears<sup>16</sup>, B.C. Shen<sup>4</sup>, C.H. Shepherd-Themistocleous<sup>8</sup>, P. Sherwood<sup>15</sup>, G.P. Sirolì<sup>2</sup>,  
A. Sittler<sup>27</sup>, A. Skillman<sup>15</sup>, A. Skuja<sup>17</sup>, A.M. Smith<sup>8</sup>, T.J. Smith<sup>28</sup>, G.A. Snow<sup>17</sup>, R. Sobie<sup>28</sup>,  
S. Söldner-Rembold<sup>10</sup>, R.W. Springer<sup>30</sup>, M. Sproston<sup>20</sup>, A. Stahl<sup>3</sup>, M. Steiert<sup>11</sup>,  
K. Stephens<sup>16</sup>, J. Steuerer<sup>27</sup>, B. Stockhausen<sup>3</sup>, D. Strom<sup>19</sup>, P. Szymanski<sup>20</sup>, R. Tafirout<sup>18</sup>,  
S.D. Talbot<sup>1</sup>, S. Tanaka<sup>24</sup>, P. Taras<sup>18</sup>, S. Tarem<sup>22</sup>, M. Thiergen<sup>10</sup>, M.A. Thomson<sup>8</sup>, E. von  
Törne<sup>3</sup>, S. Towers<sup>6</sup>, I. Trigger<sup>18</sup>, T. Tsukamoto<sup>24</sup>, E. Tsur<sup>23</sup>, A.S. Turcot<sup>9</sup>,  
M.F. Turner-Watson<sup>8</sup>, P. Utzat<sup>11</sup>, R. Van Kooten<sup>12</sup>, G. Vasseur<sup>21</sup>, M. Verzocchi<sup>10</sup>, P. Vikas<sup>18</sup>,  
M. Vinçter<sup>28</sup>, E.H. Vokurka<sup>16</sup>, F. Wäckerle<sup>10</sup>, A. Wagner<sup>27</sup>, C.P. Ward<sup>5</sup>, D.R. Ward<sup>5</sup>,  
J.J. Ward<sup>15</sup>, P.M. Watkins<sup>1</sup>, A.T. Watson<sup>1</sup>, N.K. Watson<sup>1</sup>, P.S. Wells<sup>8</sup>, N. Vermes<sup>3</sup>,  
J.S. White<sup>28</sup>, B. Wilkens<sup>10</sup>, G.W. Wilson<sup>27</sup>, J.A. Wilson<sup>1</sup>, G. Wolf<sup>26</sup>, S. Wotton<sup>5</sup>,  
T.R. Wyatt<sup>16</sup>, S. Yamashita<sup>24</sup>, G. Yekutieli<sup>26</sup>, V. Zacek<sup>18</sup>, D. Zer-Zion<sup>8</sup>

<sup>1</sup>School of Physics and Space Research, University of Birmingham, Birmingham B15 2TT, UK

<sup>2</sup>Dipartimento di Fisica dell' Università di Bologna and INFN, I-40126 Bologna, Italy

<sup>3</sup>Physikalisches Institut, Universität Bonn, D-53115 Bonn, Germany

<sup>4</sup>Department of Physics, University of California, Riverside CA 92521, USA

<sup>5</sup>Cavendish Laboratory, Cambridge CB3 0HE, UK

<sup>6</sup> Ottawa-Carleton Institute for Physics, Department of Physics, Carleton University, Ottawa, Ontario K1S 5B6, Canada

<sup>7</sup>Centre for Research in Particle Physics, Carleton University, Ottawa, Ontario K1S 5B6, Canada

<sup>8</sup>CERN, European Organisation for Particle Physics, CH-1211 Geneva 23, Switzerland

<sup>9</sup>Enrico Fermi Institute and Department of Physics, University of Chicago, Chicago IL 60637, USA

<sup>10</sup>Fakultät für Physik, Albert Ludwigs Universität, D-79104 Freiburg, Germany

<sup>11</sup>Physikalisches Institut, Universität Heidelberg, D-69120 Heidelberg, Germany

<sup>12</sup>Indiana University, Department of Physics, Swain Hall West 117, Bloomington IN 47405, USA

<sup>13</sup>Queen Mary and Westfield College, University of London, London E1 4NS, UK

<sup>14</sup>Technische Hochschule Aachen, III Physikalisches Institut, Sommerfeldstrasse 26-28, D-52056 Aachen, Germany

<sup>15</sup>University College London, London WC1E 6BT, UK

<sup>16</sup>Department of Physics, Schuster Laboratory, The University, Manchester M13 9PL, UK

<sup>17</sup>Department of Physics, University of Maryland, College Park, MD 20742, USA

<sup>18</sup>Laboratoire de Physique Nucléaire, Université de Montréal, Montréal, Quebec H3C 3J7, Canada

<sup>19</sup>University of Oregon, Department of Physics, Eugene OR 97403, USA

<sup>20</sup>Rutherford Appleton Laboratory, Chilton, Didcot, Oxfordshire OX11 0QX, UK

<sup>21</sup>CEA, DAPNIA/SPP, CE-Saclay, F-91191 Gif-sur-Yvette, France

<sup>22</sup>Department of Physics, Technion-Israel Institute of Technology, Haifa 32000, Israel

<sup>23</sup>Department of Physics and Astronomy, Tel Aviv University, Tel Aviv 69978, Israel

<sup>24</sup>International Centre for Elementary Particle Physics and Department of Physics, University of Tokyo, Tokyo 113, and Kobe University, Kobe 657, Japan

<sup>25</sup>Brunel University, Uxbridge, Middlesex UB8 3PH, UK

<sup>26</sup>Particle Physics Department, Weizmann Institute of Science, Rehovot 76100, Israel

<sup>27</sup>Universität Hamburg/DESY, II Institut für Experimental Physik, Notkestrasse 85, D-22607 Hamburg, Germany

<sup>28</sup>University of Victoria, Department of Physics, P O Box 3055, Victoria BC V8W 3P6, Canada

<sup>29</sup>University of British Columbia, Department of Physics, Vancouver BC V6T 1Z1, Canada

<sup>30</sup>University of Alberta, Department of Physics, Edmonton AB T6G 2J1, Canada

<sup>31</sup>Duke University, Dept of Physics, Durham, NC 27708-0305, USA

<sup>32</sup>Research Institute for Particle and Nuclear Physics, H-1525 Budapest, P O Box 49, Hungary

<sup>33</sup>Institute of Nuclear Research, H-4001 Debrecen, P O Box 51, Hungary

<sup>34</sup>Ludwigs-Maximilians-Universität München, Sektion Physik, Am Coulombwall 1, D-85748 Garching, Germany

<sup>a</sup> and at TRIUMF, Vancouver, Canada V6T 2A3

<sup>b</sup> and Royal Society University Research Fellow

<sup>c</sup> and Institute of Nuclear Research, Debrecen, Hungary

<sup>d</sup> and Department of Experimental Physics, Lajos Kossuth University, Debrecen, Hungary

# 1 Introduction

Semihadronic  $\tau$  decays provide an ideal laboratory to study strong interactions in a region currently not accessible to precise theoretical calculations. The decay  $\tau^- \rightarrow \pi^- \pi^- \pi^+ \nu_\tau$ <sup>1</sup>, studied in this paper, is expected by the partially conserved axial-vector current hypothesis (PCAC) and by G-parity conservation to be dominated by the axial-vector current, mainly the  $a_1$  resonance, through the decay  $\tau^- \rightarrow a_1^- \nu_\tau$  followed by the decay chain  $a_1^- \rightarrow \rho^0 \pi^-$  and  $\rho^0 \rightarrow \pi^+ \pi^-$ . The correct modelling of the  $\tau^- \rightarrow \pi^- \pi^- \pi^+ \nu_\tau$  decay dynamics is important in a variety of studies, from setting limits on the  $\tau$  neutrino mass using three-prong  $\tau$  decays to measuring the  $\tau$  polarization. Based on a previous paper [1], two different approaches have been used to study the  $\tau^- \rightarrow \pi^- \pi^- \pi^+ \nu_\tau$  decay. First, the model of Kühn and Santamaria [2], which is used to model the  $\tau^- \rightarrow \pi^- \pi^- \pi^+ \nu_\tau$  decay in TAUOLA 2.4[3], and the model of Isgur, Morningstar, and Reader [4] are both compared with the OPAL data. The  $a_1$  resonance parameters are extracted for both models, and the comparison between the data and model predicted distributions is discussed. In the second approach, a model independent analysis is used to extract the structure of the weak hadronic current using a general description of hadronic  $\tau$  decays as proposed by Kühn and Mirkes [5]. In this paper, the OPAL data collected in 1994 has been combined with the previously analysed 1992 and 1993 data, allowing the measurement of the model independent structure functions in the Dalitz plane. In addition, non-axial-vector contributions in the decay have been investigated.

A brief description of the OPAL detector is given in Section 2. The data selection, based on a likelihood method, is described in Section 3, and the theoretical framework of the  $\tau^- \rightarrow \pi^- \pi^- \pi^+ \nu_\tau$  decay is presented in Section 4. In Section 5, the two models are compared with OPAL data, and the  $a_1$  resonance parameters are extracted for each model. The structure functions are measured in section 6 and compared with model predictions. In Section 7, vector and scalar contributions to the  $\tau^- \rightarrow \pi^- \pi^- \pi^+ \nu_\tau$  decay are measured using a model independent as well as a model dependent approach. The measurement of the parity violating asymmetry parameter  $\gamma_{VA}$ , in both the model independent and model dependent frameworks, is described in Section 8. Finally, the results are summarized in Section 9.

## 2 The OPAL detector

A detailed description of the OPAL detector can be found in [6]. Only the most important elements for this analysis are mentioned here.

The innermost detector for the measurement of charged tracks is a silicon microvertex detector. Outside the microvertex detector is the central tracking system, consisting of a precision vertex drift chamber, a large volume jet chamber, and a set of  $z$ -chambers which provide measurements of the track coordinates along the beam direction. Two tracks can be resolved by the central tracking system when separated by 2.5 mm or more. The central tracking detector is immersed in a 0.435 T axial magnetic field. The momentum resolution of the jet chamber is approximately  $\sigma_{p_t}/p_t = \sqrt{0.0004 + (0.0015 p_t)^2}$ , where the momentum  $p_t$ , in GeV, is the component transverse to the beam direction. The resolution on the invariant mass of the  $3\pi$  system can be parametrized as  $\sigma(Q) = 0.011 + 0.011Q^2$ , where  $Q$  is in GeV.

---

<sup>1</sup>References in this paper to specific charge states apply to the charge conjugate states also.

The jet chamber also provides measurements of the specific energy loss of tracks in gas, with a resolution of  $\sigma(dE/dx)/(dE/dx) = 3.5\%$  for tracks with a full 159 samplings.

The electromagnetic energy is measured by a lead-glass calorimeter located outside the magnet coil and in the two end caps, while hadronic energy is measured by several planes of limited streamer tubes which are interleaved with the iron layers of the magnet return yoke. The energy resolution of the lead-glass calorimeter for 45.6 GeV electrons is  $\sigma_E/E = 2.1\%$  in the barrel region and  $\sigma_E/E = 3.1\%$  in the two end caps. The lead-glass calorimeter position resolution is about 11 mm.

A preshower system (presampler) is situated in front of the lead-glass calorimeter to improve the position and energy measurement of electromagnetic showers initiating in the magnet coil. Finally, the magnet return yoke is surrounded by a muon detector.

### 3 Selection of $\tau^- \rightarrow \pi^- \pi^- \pi^+ \nu_\tau$ decays

The selection of  $\tau^- \rightarrow \pi^- \pi^- \pi^+ \nu_\tau$  candidate events, outlined below, differs only slightly from the selection described in [1]. 114381  $\tau$  pairs have been selected, irrespective of the decay mode, from the 1992 – 1994 data sample using the  $\tau$  pair preselection described in [7]. The polar angle  $\theta_{jet}$  of each  $\tau$ -jet relative to the beam direction is determined using charged tracks and clusters in the lead-glass calorimeter. Events are selected only if the average of  $|\cos \theta_{jet}|$  for the two jets is less than 0.95. The 1992 – 1994 data sample represents 74% of the data collected at center-of-mass energies around  $\sqrt{s} = M_{Z^0}$  with the OPAL detector at LEP, and corresponds to an integrated luminosity of  $104 \text{ pb}^{-1}$ .

For the Monte Carlo simulation we have used KORALZ 4.0 [8] to produce a sample of approximately four times the number of events in the data sample. A modified version<sup>2</sup> of TAUOLA 2.4 [3] is used to generate the  $\tau$  leptons and model their decays, where the model of Kühn and Santamaria [2] is incorporated for the  $\tau^- \rightarrow \pi^- \pi^- \pi^+ \nu_\tau$  decay. The Monte Carlo generated events are passed through a full simulation of the OPAL detector [11].

The  $\tau^- \rightarrow h^- h^- h^+ \nu_\tau$  candidates have been selected from the  $\tau$  pair sample using a channel likelihood method [12]. Four variables are used in the likelihood selection to discriminate against specific background channels. Background from one-prong decays accompanied by an additional pair of electron and positron tracks from photon conversion is suppressed by using the specific energy loss ( $dE/dx$ ) to separate pions from electrons, and by using the probability of the  $\chi^2$  of a 3-dimensional vertex fit of the three tracks. Three-prong events with additional neutrals in the final state are separated from the signal channel by using the calorimetric energy sum divided by the sum of the track momenta, and also the sum of the energy of the reconstructed photons in the decay.

Reference samples have been selected for each of the four variables by applying stringent cuts on the three variables not under examination and also using information from the presampler. Although the overall agreement is satisfactory, some discrepancies between data and Monte Carlo have been observed. The Monte Carlo reference distributions have therefore been modified for the final data selection according to correction functions taken from the comparison.

---

<sup>2</sup>Unlike the standard version of TAUOLA2.4, the description of the  $\tau^- \rightarrow \pi^- \pi^- \pi^+ \pi^0 \nu_\tau$  decay is taken here from [9]. In this description, the modelling of the  $\rho$  and  $\omega$  resonances is in better agreement with the data [10].

From the selected  $\tau^- \rightarrow h^- h^- h^+ \nu_\tau$  sample, final states with kaons are suppressed by applying a cut on the specific energy loss of the tracks. Since the events have to be kinematically well reconstructed for the following analysis, a cut is also applied on the probability of the  $\chi^2$  of the three-dimensional vertex fit. The tracks of the remaining events have been constrained to the fitted vertex and the four-momenta then re-evaluated. Finally, events whose values of the reconstructed kinematical variables lie outside the physical region are rejected. A total of 7443 events pass the full selection criteria, with an estimated purity of  $(84.8 \pm 2.2)\%$ . The error is dominated by the uncertainty in the branching ratio of three-prong decays with kaons in the final state, and small discrepancies in the reference samples used for the likelihood selection between data and Monte Carlo. Estimated background contributions are itemized in table 1.

## 4 Theoretical description of the decay

The partial decay width of the decay  $\tau^- \rightarrow \pi^- \pi^- \pi^+ \nu_\tau$  can be written as

$$\begin{aligned} d\Gamma(\tau^- \rightarrow \pi^- \pi^- \pi^+ \nu_\tau) &= \sum_{\mu\nu} \frac{G_F^2}{4m_\tau} \cos^2 \theta_C L_{\mu\nu} H^{\mu\nu} d\text{PS}^{(4)} \\ &= \sum_X \frac{G_F^2}{4m_\tau} \cos^2 \theta_C L_X W_X d\text{PS}^{(4)}. \end{aligned} \quad (1)$$

$G_F$  is the Fermi constant,  $\theta_C$  the Cabbibo angle,  $m_\tau$  is the mass of the  $\tau$  lepton and  $d\text{PS}^{(4)}$  symbolizes the phase space integration. The sixteen leptonic functions  $L_X$  ( $X = A, B \dots I, SA, \dots SG$ ) are symmetric and antisymmetric combinations of the components of the leptonic tensor  $L_{\mu\nu}$ . The hadronic structure functions  $W_X$ , the subject of our measurement, are composed in the same way from the hadronic tensor  $H_{\mu\nu}$  [5].

The  $L_X$  can be calculated within the framework of the electroweak theory as functions of the  $\tau$  polarization  $P_\tau$ , the parity violating asymmetry parameter  $\gamma_{VA}$ , the invariant mass squared  $Q^2 = (p_1 + p_2 + p_3)^2$  of the hadronic system, and four decay angles  $\alpha$ ,  $\beta$ ,  $\gamma$ , and  $\cos \theta^*$ . In the Standard Model,  $\gamma_{VA} = 2g_V g_A / (g_V^2 + g_A^2) = 1$ , where  $g_V$  and  $g_A$  are the vector and axial-vector couplings in the  $\tau$  decay. The definitions of the decay angles and the detailed form of the  $L_X$  can be found in [5]. Assuming universality of the neutral current couplings as predicted by the Standard Model, the value for  $P_\tau = -0.144 \pm 0.003$  [13] is taken from a Standard Model fit which has very little dependence on measurements in the  $\tau$  sector.

The hadronic structure functions  $W_X$  depend on the four-momenta of the outgoing pions in a Lorentz invariant way, that is,  $W_X \equiv W_X(Q^2, s_1, s_2)$ . The Dalitz plot variables  $s_1$  and  $s_2$  are defined in terms of the pion momenta as  $s_1 = (p_2 + p_3)^2$  and  $s_2 = (p_1 + p_3)^2$ , with the labels chosen such that  $|\vec{p}_2| > |\vec{p}_1|$  for the two like-sign pions and  $p_3$  refers to the unlike-sign pion. In the most general description of the hadronic decay current, contributions from pseudoscalar, vector and axial-vector components have to be taken into account [14]. However, the  $\tau^- \rightarrow \pi^- \pi^- \pi^+ \nu_\tau$  decay is dominated by the axial-vector current, decaying predominantly through the decay chain  $\tau^- \rightarrow a_1^- \nu_\tau$ ,  $a_1^- \rightarrow \rho^0 \pi^-$  and  $\rho^0 \rightarrow \pi^+ \pi^-$ . Vector currents are not expected because of G-parity conservation, and pseudoscalar contributions should be small due to the PCAC hypothesis. The detailed structure of the hadronic current cannot, however, yet be predicted from theory. Furthermore, there is no way to derive the

decay structure from  $e^+e^-$  data as can be done for decays with an even number of pions in the final state through the conserved vector current hypothesis (CVC). Chiral perturbation theory methods can be used in the low energy region [15], but in the resonance region accessible here, only model predictions are available.

For this work, two techniques are used to measure the structure of the hadronic current:

1. The models give predictions for the structure functions and therefore the shapes of the distributions of the kinematic variables. The comparison between data distributions and model predictions is a measure of the quality of the model. The model parameters, such as the mass and width of the  $a_1$  meson, can also be extracted experimentally.
2. The hadronic structure functions can be extracted directly in a model independent approach. For a pure axial-vector current, only four out of 16 structure functions contribute. Using the notation defined in [5], these four structure functions are  $W_A$ ,  $W_C$ ,  $W_D$  and  $W_E$ .

## 5 Model analysis of the three-pion and two-pion mass squared distributions

Two models for the  $\tau^- \rightarrow \pi^- \pi^- \pi^+ \nu_\tau$  decay will be investigated in this analysis. These are the models of Kühn and Santamaria [2] and of Isgur et al. [4], henceforth referred to as the KS model and IMR model, respectively. The KS model uses point-like strong form factors, and incorporates only the lowest dimensional Born term in the decay amplitude. In the present analysis, the  $\rho(1450)$  is included in the KS model parametrization with a strength  $\beta_{\rho(1450)} = -0.145$ , as specified for model 1 of table 1 in ref. [2]. The IMR model, in contrast, uses strong form factors with full off-shell dependence, derived from a flux-tube breaking model [16]. The IMR model is formulated with two distinct  $a_1\rho\pi$  couplings which allows a prediction of the  $D/S$  amplitude ratio, the ratio of the amplitudes for the two possible angular momentum states of the intermediate  $\rho\pi$  state. For the IMR model, the  $K^*\bar{K}$  decay channel is allowed to contribute to the total decay width, however the pseudoscalar contribution ( $\pi(1300)$  production) is not included in the present analysis since the decay is dominated by the axial-vector current ( $W_{SA}(Q^2, s_1, s_2) = 0$ ). Several effects, such as model deficiencies and possible nonresonant contributions, are accounted for in the IMR model by employing a three parameter polynomial background term. Further details of the models can be found in [2] and [4], and a comparison of the phenomenology of the two models in [17].

Least-squares fits between predicted and data distributions have been carried out for both the models. The  $3\pi$  invariant mass squared distribution is used for both the KS and IMR model fits. For the IMR model, three  $2\pi$  invariant mass squared Dalitz-plot projections in different  $Q^2$  intervals are also used in order to measure the  $D/S$  amplitude ratio. The three Dalitz-plot projections are formed by cutting around the  $\rho$  mass squared at  $0.5 < s_1 < 0.7 \text{ GeV}^2$  and then projecting onto  $s_2$ , and vice versa, for three separate intervals in  $Q^2$ . The polynomial background term in the IMR model is employed when fitting the  $3\pi$  mass squared distribution, but not for the three  $2\pi$  mass squared projections since the cut on the  $\rho$  mass squared should suppress any possible nonresonant contributions. The non- $3\pi$  background, the selection efficiency, and the OPAL detector resolution for



each of the four histograms are estimated by analysing Monte Carlo simulated events. The non- $3\pi$  background is subtracted from each histogram, and then each histogram is corrected for efficiency. The detector resolution is accounted for by folding into the fit function the estimated resolution function. The model fits, shown in fig. 1 and summarized in table 2, will be discussed below.

The systematic errors on the  $a_1$  resonance parameters are summarized in table 3. Several checks were made concerning the background. The effects of removing the cut against kaons and the effects of using the standard version of TAUOLA 2.4 [3] to model the background from  $\tau^- \rightarrow \pi^- \pi^- \pi^+ \pi^0 \nu_\tau$  decays were investigated. For the kaon cut variations, half of the change from the nominal fits is taken as the error, reflecting the uncertainty in the corresponding branching ratios. The background fraction was also varied by  $\pm 0.020$  from the nominal value of  $f_{bgd} = 0.152$ . The effects of the detector resolution were investigated by varying the mass resolution by  $\pm 10\%$ . This has a negligible effect on the extracted parameters.

## 5.1 The KS model fits

As noted above, the  $a_1$  mass  $m_{a_1}$  and width  $\Gamma_{a_1}$  are extracted using the KS model by fitting the  $3\pi$  distribution. The normalization term for the  $3\pi$  distribution is also allowed as a free parameter. In the previous OPAL  $a_1$  model analysis [1], the  $3\pi$  and three  $2\pi$  distributions were fitted simultaneously with the KS model, using one normalization for all four histograms. There was already some evidence in [1] that the normalization for the  $2\pi$  distributions was lower than that for the  $3\pi$  distribution. This discrepancy is apparently due to the cut on the  $\rho$  mass squared when forming the  $2\pi$  distributions, since the model overestimates the  $\rho$  peak contribution. With the improved statistics of the present study, the discrepancy is even more serious. With the present data, the  $\chi^2/d.o.f.$  from a global fit of the  $3\pi$  and three  $2\pi$  distributions with the KS model is 111/49, making the extraction of the resonance parameters from a global fit unreliable.

As can be seen in fig. 1, the KS model gives a reasonably good description of the shape of the  $3\pi$  distribution. The three  $2\pi$  distributions shown for the KS model are not fits, but are derived from the parameters, including the normalization, obtained from the fit to the  $3\pi$  distribution. The model is significantly high in the region of the  $\rho$  peak of the  $2\pi$  distributions. If the three  $2\pi$  distributions are fitted separately from the  $3\pi$  distribution, with the  $a_1$  mass and width fixed at the values determined from the fit to the  $3\pi$  distribution and only the normalization allowed as a free parameter, the normalization of the fitted  $2\pi$  distributions is found to be approximately 10% lower than that of the  $3\pi$  distribution. This suggests the presence of contributions to the decay not predicted by the model. Such contributions would affect the  $3\pi$  and  $2\pi$  plots differently because of the cut on the  $\rho$  resonance region when forming the  $2\pi$  plots.

## 5.2 The IMR model fits

With the IMR model fit, the normalization is applied only to the part of the  $3\pi$  distribution lying above the polynomial background. As noted in [1], this serves to compensate the normalization discrepancy between the  $3\pi$  and the three  $2\pi$  distributions, for which the polynomial background is not employed. A global analysis of all four histograms can therefore be carried out with the IMR model. In order to extract the D/S amplitude ratio, the strengths

of the  $f_{a_1\rho\pi}$  and  $g_{a_1\rho\pi}$  form factors (see ref. [4]) are allowed to vary independently from their nominal flux-tube breaking model values. The relative strengths of these two form factors are most sensitive to the shapes of the three  $2\pi$  distributions. All other form factor parameters are held fixed at their nominal values,  $\beta_{HO} = 0.4$  GeV and  $\gamma_o = 0.39$ . For the fits to the data with the IMR model, the free parameters of the fit are the  $a_1$  mass, the overall normalization, the three parameters which govern the strength and shape of the polynomial background underlying the  $3\pi$  distribution, and the two strengths for the  $f_{a_1\rho\pi}$  and  $g_{a_1\rho\pi}$  form factors.

As can be seen in fig. 1, the IMR model also gives a reasonably good description of the  $3\pi$  distribution, with  $\chi^2 = 34.3$  for 23 bins. As mentioned above, the polynomial background term employed by the IMR model serves as a correction for the inconsistencies seen with the KS model fit. However, if the polynomial background is excluded from the IMR model, the  $\chi^2$  increases to 138.7 for 48 *d.o.f.* and the extracted parameters shift significantly. The three parameters for the polynomial background of the IMR model fit are  $c_1 = -1.86$ ,  $c_2 = 5.65$ , and  $c_3 = -0.78$  (see [4] for the parametrization of the polynomial background). These three parameters are highly correlated and have errors ranging from 50% to 130%. The normalization for the polynomial background term is such that the background contribution is  $(13.8 \pm 2.4)\%$  of the total  $3\pi$  distribution, where the error is statistical only. As can be seen in table 2, the  $a_1$  mass and width extracted from the IMR model fit differ significantly from those extracted from the KS model fit. This has been shown in [17] to be due primarily to the employment of off-shell dependent strong form factors by the IMR model, in contrast to the pointlike strong form factors used by the KS model. The overall features of the  $2\pi$  distributions are also reproduced by the IMR model. As can be seen in fig. 1(c), however, the model is systematically low in the low  $s_{1,2}$  region. The results for the strong decay on-shell  $a_1\rho\pi$  form factors and the  $D/S$  amplitude ratio of the IMR model fit are  $f_{a_1\rho\pi}(m_{a_1}^2, m_\rho^2) = 5.0 \pm 0.1$  GeV,  $g_{a_1\rho\pi}(m_{a_1}^2, m_\rho^2) = 3.7 \pm 1.3$  GeV, and  $D/S = -0.10 \pm 0.02 \pm 0.02$ . These values are in reasonable agreement with the predictions of  $f_{a_1\rho\pi}(m_{a_1}^2, m_\rho^2) = 4.8$  GeV,  $g_{a_1\rho\pi}(m_{a_1}^2, m_\rho^2) = 6.0$  GeV, and  $D/S = -0.15$  from the flux-tube breaking model [4], which is used by the IMR model to compute the strong form factors.

### 5.3 Further discussion of the model fits

The problems noted above with the model fits to the data can be seen more clearly if we investigate the  $2\pi$  mass squared Dalitz-plot projection with no cuts on either the  $a_1$  mass or the  $\rho$  mass. The data have been overlaid by the two models in fig. 2, with the model parameters held fixed at their nominal best fit values. The normalization for the KS model was taken from the fit to the  $3\pi$  distribution, and the normalization for the IMR model was taken from the global fit. The  $Q^2$  dependent polynomial background term of the IMR model, determined from the  $3\pi$  distribution in the IMR global fit, has also been included for that model.

It is clearly evident that the KS model overestimates the  $\rho$  peak contribution relative to the high and low  $s_1$  regions, especially the low  $s_1$  region. The total  $\chi^2$  for the KS model overlay is 95.4 for 28 bins. The IMR model gives an improved description of the uncut  $2\pi$  distribution, although it remains systematically low in the low  $s_1$  region. The IMR model's inclusion of the  $g_{a_1\rho\pi}$  term is responsible for the steeper rise toward the low  $s_1$  region. The total  $\chi^2$  for the IMR model overlay is 50.2 for 28 bins. Without the inclusion of the polynomial background term, the total  $\chi^2$  for the IMR model overlay increases to 115 for 28 bins.

To investigate whether the apparent poor modelling of the data in the low  $s_1$  region could be due to incorrect modelling of the  $\tau^- \rightarrow \pi^- \pi^- \pi^+ \pi^0 \nu_\tau$  decay mode, which is the predominant background in this region, a data selection was generated with the purity improved to 89.8 %. The improvement in purity was aimed primarily at reducing the background due to  $\tau^- \rightarrow \pi^- \pi^- \pi^+ \pi^0 \nu_\tau$  decays. The ratio of data events to Monte Carlo simulated events remains unchanged in the low  $s_1$  region with this selection, which provides evidence that the discrepancy of the models with the data in the low  $s_1$  region is not due to incorrect background modelling.

It should be pointed out that the  $Q^2$  dependence of the polynomial background term of the IMR model has largely been integrated out when it is projected onto the  $s_1$  axis for the  $2\pi$  mass projection. The residual  $s_1$  dependent shape is due to the kinematic boundaries of the physical region in  $(Q^2, s_1, s_2)$  space. Also, since the polynomial background term is a function of  $Q^2$  only, the IMR model is of limited use for Monte Carlo simulation of the  $\tau^- \rightarrow \pi^- \pi^- \pi^+ \pi^0 \nu_\tau$  decay. The limited available statistics prohibit a reliable determination of the full  $(Q^2, s_1, s_2)$  dependence of the background term. Nonetheless, in the framework of the IMR model it is evident that the data do require some sort of additional term with a magnitude of  $(13.8 \pm 2.4)\%$ .

The high model dependence of the measured  $a_1$  resonance parameters, and also the failure of either model to provide a completely satisfactory description of the data, strongly suggest that caution must be exercised when carrying out measurements which rely on models for predicting the decay dynamics in  $\tau^- \rightarrow \pi^- \pi^- \pi^+ \pi^0 \nu_\tau$ .

## 6 Extraction of the structure functions

The hadronic decay current can be measured in a model independent way by extracting the hadronic structure functions directly. This can be done in two steps.

1. As the axial-vector current dominates the decay, all structure functions other than  $W_A$ ,  $W_C$ ,  $W_D$ , and  $W_E$  can be fixed to zero. To measure the  $Q^2$ -dependence, the structure functions are integrated over the Dalitz plane,

$$w_X(Q^2) = \int W_X(s_1, s_2, Q^2) ds_1 ds_2, \quad (2)$$

and the selected events are put into nine equal sized  $Q^2$  bins between 0.5 and 2.75 GeV<sup>2</sup>. No binning is used for the angles.

2. To study the full structure of the hadronic decay current, and accepting larger errors, the events are binned not only in  $Q^2$  but also in  $(s_1, s_2)$ , as shown in table 4. This is only possible due to the increased data sample compared with [1]. Structure functions that include scalar ( $W_{SB}$  and  $W_{SD}$ ) and vector ( $W_F$ ,  $W_G$ ,  $W_H$ , and  $W_I$ ) contributions have also been taken into account, neglecting only those that are pure vector ( $W_B$ ), pure scalar ( $W_{SA}$ ), or interference terms between vector and scalar currents ( $W_{SF}$ ) as they are expected to be very small. Since the respective angular dependences of  $W_G$  and  $W_{SD}$  and of  $W_I$  and  $W_{SB}$  are very similar, they cannot be separated with the available data sample. Therefore they are combined in the fit parameters  $X_1 = -\bar{K}_3/\bar{K}_2 W_G - W_{SD}$  and  $X_2 = -\bar{K}_3/\bar{K}_2 W_I + W_{SB}$  (See [5] for the definitions of  $\bar{K}_3$  and  $\bar{K}_2$ ).

Both measurements can be made, following the method described in [1], by applying an extended maximum likelihood fit [18] to the data events. With  $z$  representing the kinematic variables  $Q^2$ ,  $s_1$ ,  $s_2$ ,  $\cos \theta^*$ ,  $\cos \beta$ , and  $\gamma$ , and  $dz = dQ^2 ds_1 ds_2 d \cos \theta^* d \cos \beta d \gamma$ , the likelihood function can be written as

$$(\ln \mathcal{L})_j = \sum_i^{N_j} \ln \left( \frac{d\Gamma}{dz} (z_i; W_X^j) \frac{N}{C_{corr} \Gamma_{3\pi}} \right) - \Gamma_{\Delta_j} (W_A^j) \frac{N}{C_{corr} \Gamma_{3\pi}}. \quad (3)$$

Here the  $W_X^j$  are the average values of the structure functions  $W_X$  within bin  $j$  (referring only to  $Q^2$  in the first step and to  $Q^2$ ,  $s_1$ ,  $s_2$  in the second step). They are the parameters of the fit.  $N_j$  is the number of events in bin  $j$  and  $N$  is the total number of selected events.  $\Gamma_{3\pi}$  is the partial decay width of the  $\tau$  decay into three pions, calculated from ref. [13] ( $\Gamma_{3\pi}/\Gamma_{tot} = 9.31\%$ , with  $\Gamma_{3\pi} = 2.11 \times 10^{-4}$  eV). The factor  $C_{corr}$  (with  $C_{corr} = 0.996$ ) corrects  $\Gamma_{3\pi}$  for events with  $Q^2$  outside of the selected range of  $0.5 \text{ GeV}^2 < Q^2 < 2.75 \text{ GeV}^2$ . The decay distribution  $d\Gamma/dz$  is defined in eq. (1). The normalization term  $\Gamma_{\Delta_j}$  is the integral of  $d\Gamma/dz$  over the full ranges of the kinematic angles and the bin width. Because of the increased value of  $\text{BR}(\tau^- \rightarrow \pi^- \pi^- \pi^+ \nu_\tau)$  relative to the value taken in the previous analysis [1], the integral and therefore the values of the structure functions have also increased.

The detector resolution has been taken into account by applying a smearing function to each of the kinematic variables on an event by event basis. To correct for migration effects between neighbouring bins, a bin to bin correction is included [19]. A smooth efficiency correction derived from Monte Carlo is incorporated in the fit by multiplying  $d\Gamma/dz$  by a correction function for each of the respective four (in the case of  $w_X(Q^2)$ ) and six (for the  $W_X(Q^2, s_1, s_2)$  measurement) kinematic variables. The background is included in the fit by replacing  $d\Gamma/dz$  in eq. (3) by

$$f_{sig} \frac{d\Gamma}{dz}(z; W_X) + f_{bgd} \frac{d\Gamma}{dz}(z; W_X^{bgd}), \quad (4)$$

where  $f_{sig} = 1 - f_{bgd}$  and  $f_{bgd}$  are the overall fractions of signal and background, and  $W_X^{bgd}$  are the background structure functions taken from the Monte Carlo prediction. These background structure functions have no physical meaning — they are simply a way to include the background in the fit function.

## 6.1 Results

The results of the measurements of the hadronic structure functions  $w_A$ ,  $w_C$ ,  $w_D$ , and  $w_E$  are presented in fig. 3 and table 5. The measurements of the hadronic structure functions  $W_A$ ,  $W_C$ ,  $W_D$ ,  $W_E$ ,  $W_F$ ,  $W_H$ ,  $X_1$ , and  $X_2$  are summarized in tables 6 and 7.

The systematic errors have been derived for both measurements in a similar way. The uncertainty in the background and migration between bins dominate the systematic errors. The different contributions have been estimated in the same way as described in section 5. The background fraction  $f_{bgd}$  has been changed in the fit by  $\pm 0.020$ . The cut against three-prong events with kaons was removed and half of the change is quoted as the error. To derive the uncertainty from the background description, the change from varying the background structure functions  $W_X^{bgd}$  within their statistical errors and the change obtained

when using the original version of TAUOLA 2.4 for the description of the background from  $\tau^- \rightarrow \pi^- \pi^- \pi^+ \pi^0 \nu_\tau$  decays are added in quadrature.

Effects due to detector efficiency and resolution were estimated by varying the correction functions for the efficiencies within one standard deviation and by increasing by 10% the widths of the Gaussians for the resolution simultaneously for all kinematic variables. The migration corrections have been varied within the errors. Furthermore, the value taken for  $P_\tau$  has been varied within the errors (see section 4).

Table 8 itemizes the estimated systematic error contributions averaged over all bins. The systematic error determined for each bin separately is used in tables 5–7, where the measured values including statistical and systematic errors are given bin by bin. The correlations between the values of the structure functions typically range between  $-15\%$  and  $+15\%$ .

## 6.2 Comparison of the structure functions with the model predictions

In fig. 4 the measured structure functions  $w_A$ ,  $w_C$ ,  $w_D$ , and  $w_E$  are compared with the KS and IMR model predictions using the fit parameters extracted in section 5. For the IMR model, the polynomial background term is included in  $w_A$ . The ratio  $w_X/w_A$ , which is only weakly dependent on  $m_{a_1}$  and  $\Gamma_{a_1}$ , is plotted for each of the other three structure functions  $w_C$ ,  $w_D$ , and  $w_E$ . For  $w_A$ , which is closely related to the  $a_1$  resonance shape, the KS model fits the data distribution very well, with  $\chi_{KS}^2 = 6.2$  for 9 bins. The IMR model, however, shows some discrepancies, with  $\chi_{IMR}^2 = 16.9$  for 9 bins. The structure visible in the IMR model prediction at  $Q^2 = 1.9 \text{ GeV}^2$ , which is related to the  $a_1 \rightarrow K^* \bar{K}$  decay channel, is not visible in the data. This suggests that the IMR modelling of that decay channel is not correct. For the description of  $w_C/w_A$ ,  $w_D/w_A$ , and  $w_E/w_A$ , both models agree well with the measurement, with  $\chi_{KS}^2 = 19.6$  for 27 bins and  $\chi_{IMR}^2 = 17.6$  for 27 bins.

To demonstrate how the structure functions are distributed in the Dalitz plane, the axial-vector structure functions  $W_A$ ,  $W_C$ ,  $W_D$ , and  $W_E$  are shown in fig. 5 in comparison with the KS model. The results for the KS model are evaluated at  $Q^2 = 1.3 \text{ GeV}^2$ , while the fit results are integrated over the range  $1.21 \text{ GeV}^2 < Q^2 < 1.44 \text{ GeV}^2$ . The structure functions  $W_F$ ,  $W_H$ ,  $X_1$ , and  $X_2$  all vanish for the model predictions.

## 7 Non-axial-vector contributions

If there are non-axial-vector contributions in the hadronic decay current, they should be visible in the angular distributions and therefore manifest themselves in the hadronic structure functions  $W_F$  and  $W_H$  and in the fit parameters  $X_1$  and  $X_2$ . The fit results, shown in fig. 6, can therefore be compared to the null prediction of vanishing vector and scalar components. This leads to  $\chi^2 = 81.2$  for 84 *d.o.f.* No deviation from a pure axial-vector current is observed.

For a quantitative measurement of the non-axial-vector contributions, a different method has been applied. Because of strong correlations between  $W_A$ ,  $W_B$  and  $W_{SA}$  the fit result for  $W_A^{fit}$  includes possible scalar or vector contributions. The pure axial-vector part of  $W_A$  can be calculated from  $W_C$ ,  $W_D$  and  $W_E$  ( $W_A^2 = W_C^2 + W_D^2 + W_E^2$ ) since these structure functions are independent of vector or scalar contributions.<sup>3</sup> An estimate of the non-axial-vector components can be calculated as  $\Delta^{non-AV} = W_A^{fit} - \sqrt{W_C^2 + W_D^2 + W_E^2}$ . This

<sup>3</sup> $W_{SF}$ , a combination of vector and scalar components, is neglected here.

leads to the first model independent measurement of non-axial-vector contributions, with an upper limit at the 95% confidence level of

$$\frac{\Gamma^{non-AV}(\tau^- \rightarrow \pi^- \pi^- \pi^+ \nu_\tau)}{\Gamma^{tot}(\tau^- \rightarrow \pi^- \pi^- \pi^+ \nu_\tau)} < 26.1\%.$$

The deviation from zero non-axial-vector contributions was also measured using samples of Monte Carlo generated events which include different amounts of non-axial-vector contributions. In addition to the systematic errors considered in the previous section, an error of 14% from this test with Monte Carlo events has been included.

The contribution of a scalar component to the decay can be measured model dependently under the assumption that it can be fully described through the decay chain  $\tau^- \rightarrow \pi^-(1300)\nu_\tau$ ,  $\pi^-(1300) \rightarrow \rho^0 \pi^-$  and  $\rho^0 \rightarrow \pi^+ \pi^-$ . In this approach, the axial-vector current is described by the KS or IMR model. The scalar contribution can be incorporated in both models; only the strength of the scalar current is not fixed. The structure functions in eq. 3 can now be replaced by the model predictions when performing the extended maximum likelihood fit, with the contribution from the scalar current being the only fit parameter. The result of the fit shows no evidence for a scalar current, and leads to the 95% confidence level upper limit

$$\frac{\Gamma^{scalar}(\tau^- \rightarrow \pi^-(1300)\nu_\tau)}{\Gamma^{tot}(\tau^- \rightarrow \pi^- \pi^- \pi^+ \nu_\tau)} < 0.84\%,$$

in agreement with a model dependent analysis by ARGUS [20]. In addition to the systematic errors described above, the dependence on model (KS or IMR) used for the axial-vector part of the decay has been investigated and included in the systematic error.

## 8 The parity violating asymmetry parameter $\gamma_{VA}$

As explained in section 4, the leptonic current depends on the parity violating asymmetry parameter  $\gamma_{VA}$ . For the measurement of the hadronic structure functions described in the previous sections, the value was fixed at the Standard Model value of  $\gamma_{VA} = 1$ . If instead  $\gamma_{VA}$  is varied in the fit along with the structure functions, the parity violating asymmetry parameter can be measured. Non-axial-vector contributions are neglected here. The likelihood function summed over all bins is shown in fig. 7, leading to a model independent measurement of  $\gamma_{VA} = 1.29 \pm 0.26 \pm 0.11$ , consistent with the Standard Model prediction of  $\gamma_{VA} = 1$  for left-handed tau neutrinos. This result is in agreement with a recent measurement by SLD [21] where the sign of the helicity of the tau neutrino has also been measured model independently, and with other more precise measurements based on different techniques [22]. The systematic error is derived from the same variations described above. The dominant effects come from the uncertainty in the detector resolution and the background, especially from three-prong events with kaons in the final state. The error contributions are summarized in table 9.

The model independent result can be compared to the model dependent measurements when the fit parameters  $W_X^j$  in eq. (3) are replaced by the hadronic structure functions derived from the two models. The model dependent values obtained for the parity violating asymmetry parameter are  $\gamma_{VA}^{KS} = 0.87 \pm 0.16 \pm 0.04$  for the KS model and  $\gamma_{VA}^{IMR} = 1.20 \pm 0.21 \pm 0.14$  for the IMR model. The systematic errors for the model dependent measurements have been

derived from the same variations described above, and also by varying the model parameters within the errors given in section 5. A summary of the different error contributions is given in table 9. The largest systematic error contribution for the IMR model is due to the uncertainty in the  $D/S$  amplitude ratio. No variation of this parameter is possible for the KS model. The strong model dependence demonstrated in the measurements again emphasizes that caution must be exercised when carrying out precision measurements which rely on model descriptions for the hadronic decay current in  $\tau^- \rightarrow \pi^- \pi^- \pi^+ \nu_\tau$ .

## 9 Conclusions

We have studied the structure of the decay  $\tau^- \rightarrow \pi^- \pi^- \pi^+ \nu_\tau$  using two different approaches. First, the models of Kühn and Santamaria [2] and of Isgur et al. [4] have been used to fit the distributions of the  $3\pi$  invariant mass squared as well as  $2\pi$  mass projections of the corresponding Dalitz plot. The  $a_1$  resonance model parameters have been measured for both models, and are summarized in table 2. Both models describe reasonably well the shape of the  $3\pi$  mass squared distribution. For the uncut  $2\pi$  mass projection, however, the KS model overestimates the  $\rho$  peak, and both models underestimate the low  $s_{1,2}$  region. By including the  $Q^2$  dependent polynomial background term in the  $2\pi$  mass projection for the IMR model, the agreement with the data is improved. This suggests the possibility that some additional contribution to the decay, other than the  $a_1$  intermediate resonance, of magnitude  $(13.8 \pm 2.4)\%$  is required by the data within the framework of that model. The failure of either model to provide a completely satisfactory description of the data strongly suggests that caution must be used when carrying out measurements which rely on model descriptions for the decay dynamics in  $\tau^- \rightarrow \pi^- \pi^- \pi^+ \nu_\tau$ , and calls for further theoretical input to the modelling of this decay.

A model independent measurement has been presented of the structure functions  $w_A, w_C, w_D$ , and  $w_E$ , as well as  $W_A, W_C, W_D, W_E, W_F, W_H, X_1$ , and  $X_2$ . No evidence for non-axial-vector contributions in the decay current has been found. In the model independent approach we have obtained, at the 95% confidence level,

$$\frac{\Gamma^{non-AV}(\tau^- \rightarrow \pi^- \pi^- \pi^+ \nu_\tau)}{\Gamma^{tot}(\tau^- \rightarrow \pi^- \pi^- \pi^+ \nu_\tau)} < 26.1\%.$$

When model descriptions for the decay are used, we obtain as the 95% confidence level upper limit

$$\frac{\Gamma^{scalar}(\tau^- \rightarrow \pi^-(1300) \nu_\tau)}{\Gamma^{tot}(\tau^- \rightarrow \pi^- \pi^- \pi^+ \nu_\tau)} < 0.84\%.$$

Finally, the value for the parity violating asymmetry parameter has been determined in a model independent way to be

$$\gamma_{VA} = 1.29 \pm 0.26 \pm 0.11,$$

which is consistent with the Standard Model prediction of  $\gamma_{VA} = 1$  for left-handed tau neutrinos. The model dependent values have also been measured, but demonstrate a strong model dependence in the value obtained.

## Acknowledgements

We would like to thank J. H. Kühn and E. Mirkes for many useful discussions. We also particularly wish to thank the SL Division for the efficient operation of the LEP accelerator and for their continuing close cooperation with our experimental group. In addition to the support staff at our own institutions we are pleased to acknowledge the  
Department of Energy, USA,  
National Science Foundation, USA,  
Particle Physics and Astronomy Research Council, UK,  
Natural Sciences and Engineering Research Council, Canada,  
Israel Science Foundation, administered by the Israel Academy of Science and Humanities,  
Minerva Gesellschaft,  
Japanese Ministry of Education, Science and Culture (the Monbusho) and a grant under the Monbusho International Science Research Program,  
German Israeli Bi-national Science Foundation (GIF),  
Direction des Sciences de la Matière du Commissariat à l'Énergie Atomique, France,  
Bundesministerium für Bildung, Wissenschaft, Forschung und Technologie, Germany,  
National Research Council of Canada,  
Hungarian Foundation for Scientific Research, OTKA T-016660, and OTKA F-015089.

## References

- [1] R. Akers *et al.*, OPAL Collab., *Z. Phys.* **C67** (1995) 45.
- [2] J. H. Kühn and A. Santamaria, *Z. Phys.* **C48** (1990) 445.
- [3] S. Jadach, Z. Wąs, R. Decker and J. H. Kühn, *Comp. Phys. Comm.* **76** (1993) 361.
- [4] N. Isgur, C. Morningstar and C. Reader, *Phys. Rev.* **D39** (1989) 1357.
- [5] J. H. Kühn and E. Mirkes, *Z. Phys.* **C56** (1992) 661.
- [6] K. Ahmet *et al.*, OPAL Collab., *Nucl. Instr. Meth.* **A305** (1991) 275;  
P. P. Allport *et al.*, OPAL Collab., *Nucl. Instr. Meth.* **A324** (1993) 34;  
P. P. Allport *et al.*, OPAL Collab., *Nucl. Instr. Meth.* **A346** (1994) 476.
- [7] M. Z. Akrawy *et al.*, OPAL Collab., *Phys. Lett.* **B247** (1990) 458.
- [8] S. Jadach, B. F. L. Ward and Z. Wąs, *Comp. Phys. Comm.* **79** (1994) 503.
- [9] R. Decker *et al.*, *Z. Phys.* **C70** (1996) 247.
- [10] H. Albrecht *et al.*, ARGUS Collab., *Phys. Lett.* **B185** (1987) 223; *Phys. Lett.* **B260** (1991) 259.
- [11] J. Allison *et al.*, *Nucl. Instr. Meth.* **A317** (1992) 47.



- [12] P. E. Condon and P. L. Cowell, *Phys. Rev.* **D9** (1974) 2558.
- [13] Review of Particle Physics, R. M. Barnett *et al.*, *Phys. Rev.* **D54** (1996) 91.
- [14] Y. S. Tsai, *Phys. Rev.* **D4** (1971) 2821.
- [15] G. Colangelo *et al.*, TTP96-02 (1996).
- [16] R. Kokoski and N. Isgur, *Phys. Rev.* **D35** (1987) 907.
- [17] P. R. Poffenberger, *Z. Phys.* **C71** (1996) 579.
- [18] R. J. Barlow: *Statistics*, New York: John Wiley & Sons (1989).
- [19] V. Blobel, DESY 84-118 (1984);  
V. Blobel, *Proceedings of the 1984 CERN School of Computing*, CERN 85-02 (1984).
- [20] H. Albrecht *et al.*, ARGUS Collab., *Phys. Lett.* **B349** (1995) 576.
- [21] K. Abe *et al.*, SLD Collab., SLAC-PUB-7333.
- [22] D. Buskulic *et al.*, ALEPH Collab., *Phys. Lett.* **B346** (1995) 379;  
H. Albrecht *et al.*, ARGUS Collab., *Phys. Lett.* **B349** (1995) 576.

decay channel	background fraction
$\tau^- \rightarrow \pi^- \pi^- \pi^+ \pi^0 \nu_\tau$	$(11.7 \pm 0.5) \%$
$\tau^- \rightarrow K^- \pi^- \pi^+ \nu_\tau$	$(2.3 \pm 0.3) \%$
$\tau^- \rightarrow \pi^- K^- K^+ \nu_\tau$	$(0.5 \pm 0.1) \%$
$\tau^- \rightarrow \pi^- \pi^- \pi^+ 2\pi^0 \nu_\tau$	$(0.3 \pm 0.1) \%$
others	$(0.4 \pm 0.1) \%$

Table 1: *Estimated background fractions in the final data sample. The errors are the statistical errors from the Monte Carlo only.*

	Kühn et al. [2]	Isgur et al. [4]
$m_{a_1}$ (GeV)	$1.262 \pm 0.009 \pm 0.007$	$1.210 \pm 0.007 \pm 0.002$
$\Gamma_{a_1}$ (GeV)	$0.621 \pm 0.032 \pm 0.058$	$0.457 \pm 0.015 \pm 0.017$
D/S amplitude ratio	—	$-0.10 \pm 0.02 \pm 0.02$
$\chi^2/d.o.f.$	25.2/20 ( $3\pi$ ) 111/49 (global)	— 91.9/45 (global)
polynomial background fraction	—	$(13.8 \pm 2.4) \%$

Table 2: *Model parameters extracted from fitting the KS and IMR models to OPAL data. The errors quoted are statistical followed by systematic. Note that  $\Gamma_{a_1}$  and the D/S amplitude ratio for the IMR model are calculated quantities, not parameters of the fit. Also listed is the polynomial background fraction for the IMR model.*

	KS model error		IMR model error		
	$\Delta m_a$ (GeV)	$\Delta \Gamma_a$ (GeV)	$\Delta m_a$ (GeV)	$\Delta \Gamma_a$ (GeV)	$\Delta D/S$
Kaon channels	$\pm 0.002$	$\pm 0.014$	$\pm 0.001$	$\pm 0.005$	$\pm 0.01$
$\tau^- \rightarrow \pi^- \pi^- \pi^+ \pi^0 \nu_\tau$ decay modelling	$\pm 0.006$	$\pm 0.055$	$\pm 0.001$	$\pm 0.016$	$\pm 0.01$
Background fraction	$\pm 0.001$	$\pm 0.011$	$\pm 0.001$	$< 0.001$	$< 0.01$
Detector resolution	$\pm 0.003$	$\pm 0.007$	$\pm 0.001$	$\pm 0.002$	$< 0.01$
Total systematic error	$\pm 0.007$	$\pm 0.058$	$\pm 0.002$	$\pm 0.017$	$\pm 0.02$
Statistical error	$\pm 0.009$	$\pm 0.032$	$\pm 0.007$	$\pm 0.015$	$\pm 0.02$

Table 3: *Estimated error contributions for each of the KS and IMR model fits.*

	$\sqrt{Q^2}$ in (GeV)	$s_1$ in (GeV <sup>2</sup> )	$s_2$ in (GeV <sup>2</sup> )	$N_j$
Bin 1	0.8 – 1.0	$s_1^{min} - 0.4$	$s_2^{min} - s_1$	417
Bin 2	0.8 – 1.0	0.4 – 0.5	$s_2^{min} - s_1$	462
Bin 3	0.8 – 1.0	$0.5 - s_1^{max}$	$s_2^{min} - 0.25$	359
Bin 4	0.8 – 1.0	$0.5 - s_1^{max}$	$0.25 - s_1$	140
Bin 5	1.0 – 1.1	$s_1^{min} - 0.5$	$s_2^{min} - s_1$	392
Bin 6	1.0 – 1.1	0.5 – 0.65	$s_2^{min} - 0.35$	537
Bin 7	1.0 – 1.1	0.5 – 0.65	$0.35 - s_1$	372
Bin 8	1.0 – 1.1	$0.65 - s_1^{max}$	$s_2^{min} - s_1$	315
Bin 9	1.1 – 1.2	$s_1^{min} - 0.5$	$s_2^{min} - s_1$	247
Bin 10	1.1 – 1.2	0.5 – 0.7	$s_2^{min} - 0.3$	352
Bin 11	1.1 – 1.2	0.5 – 0.7	$0.3 - 0.5$	377
Bin 12	1.1 – 1.2	0.5 – 0.7	$0.5 - s_1$	324
Bin 13	1.1 – 1.2	$0.7 - s_1^{max}$	$s_2^{min} - s_1$	408
Bin 14	1.2 – 1.4	$s_1^{min} - 0.5$	$s_2^{min} - s_1$	137
Bin 15	1.2 – 1.4	0.5 – 0.7	$s_2^{min} - 0.45$	461
Bin 16	1.2 – 1.4	0.5 – 0.7	$0.45 - s_1$	339
Bin 17	1.2 – 1.4	$0.7 - s_1^{max}$	$s_2^{min} - 0.6$	743
Bin 18	1.2 – 1.4	$0.7 - s_1^{max}$	$0.6 - s_1$	434
Bin 19	1.4 – 1.7	$s_1^{min} - 0.7$	$s_2^{min} - s_1$	111
Bin 20	1.4 – 1.7	$0.7 - s_1^{max}$	$s_2^{min} - 0.6$	173
Bin 21	1.4 – 1.7	$0.7 - s_1^{max}$	$0.6 - s_1$	209

Table 4: Binning employed in  $Q^2$ ,  $s_1$ , and  $s_2$  for the second structure function fit.  $s_1^{min/max}$  and  $s_2^{min/max}$  are the values at the phase space boundaries. Only the lower half of the Dalitz plane ( $s_1 > s_2$ ) is used in the fit.

$Q^2$ (GeV <sup>2</sup> )	$N_j$	$w_A$ (GeV <sup>4</sup> )			$w_C$ (GeV <sup>4</sup> )		
0.5 – 0.75	334	32	±6	±18	0	±34	±21
0.75 – 1.00	1178	670	±20	±36	630	±200	±70
1.00 – 1.25	1920	2316	±59	±77	1800	±530	±60
1.25 – 1.50	1793	3870	±100	±150	3800	±1100	±200
1.50 – 1.75	1133	4290	±130	±170	5900	±1900	±700
1.75 – 2.00	655	4140	±180	±260	2900	±1900	±500
2.00 – 2.25	269	3400	±220	±270	7300	±3800	±1400
2.25 – 2.50	106	3330	±350	±390	3300	±7400	±5700
2.50 – 2.75	55	2170	±290	±360	9400	±6800	±2800
$Q^2$ (GeV <sup>2</sup> )	$N_j$	$w_D$ (GeV <sup>4</sup> )			$w_E$ (GeV <sup>4</sup> )		
0.5 – 0.75	334	24	±36	±24	–22	±27	±6
0.75 – 1.00	1178	160	±180	±30	20	±120	±50
1.00 – 1.25	1920	1430	±530	±100	–220	±270	±70
1.25 – 1.50	1793	2500	±1000	±500	–600	±430	±100
1.50 – 1.75	1133	2900	±1700	±1000	–1180	±540	±180
1.75 – 2.00	655	900	±2500	±800	–40	±650	±240
2.00 – 2.25	269	800	±3800	±500	–520	±770	±360
2.25 – 2.50	106	6600	±7200	±3300	–900	±1300	±400
2.50 – 2.75	55	–4300	±5900	±2400	1200	±1000	±700

Table 5: *The hadronic structure functions  $w_A$ ,  $w_C$ ,  $w_D$ , and  $w_E$  as measured in each  $Q^2$  bin. For each structure function, the central value, statistical and systematic errors are given.  $N_j$  is the number of decays in the given  $Q^2$  bin. The contributions shown in table 8 are included in the systematic errors.*

	$W_A$			$W_C$		
Bin 1	1100	$\pm 100$	$\pm 500$	800	$\pm 680$	$\pm 250$
Bin 2	3100	$\pm 180$	$\pm 390$	3000	$\pm 1200$	$\pm 400$
Bin 3	8230	$\pm 500$	$\pm 830$	7800	$\pm 4000$	$\pm 2300$
Bin 4	9200	$\pm 800$	$\pm 3300$	2800	$\pm 7800$	$\pm 3800$
Bin 5	2780	$\pm 140$	$\pm 540$	1500	$\pm 1600$	$\pm 600$
Bin 6	10090	$\pm 500$	$\pm 750$	10300	$\pm 4000$	$\pm 1200$
Bin 7	12130	$\pm 680$	$\pm 1410$	1600	$\pm 5500$	$\pm 2800$
Bin 8	5630	$\pm 370$	$\pm 920$	3100	$\pm 3200$	$\pm 900$
Bin 9	3870	$\pm 320$	$\pm 880$	3800	$\pm 3100$	$\pm 1100$
Bin 10	9080	$\pm 560$	$\pm 740$	2900	$\pm 4600$	$\pm 700$
Bin 11	8000	$\pm 460$	$\pm 920$	14700	$\pm 4100$	$\pm 2100$
Bin 12	24700	$\pm 1500$	$\pm 2500$	37000	$\pm 13000$	$\pm 5900$
Bin 13	3290	$\pm 200$	$\pm 390$	3300	$\pm 2000$	$\pm 600$
Bin 14	1940	$\pm 210$	$\pm 670$	700	$\pm 2600$	$\pm 1300$
Bin 15	5830	$\pm 310$	$\pm 750$	1900	$\pm 4000$	$\pm 900$
Bin 16	11500	$\pm 700$	$\pm 1500$	13900	$\pm 8300$	$\pm 2100$
Bin 17	2810	$\pm 120$	$\pm 230$	2900	$\pm 1500$	$\pm 400$
Bin 18	9900	$\pm 500$	$\pm 1100$	15900	$\pm 6700$	$\pm 1900$
Bin 19	2750	$\pm 290$	$\pm 530$	-6500	$\pm 5100$	$\pm 1400$
Bin 20	1010	$\pm 90$	$\pm 220$	1800	$\pm 1500$	$\pm 400$
Bin 21	2940	$\pm 220$	$\pm 730$	6100	$\pm 3700$	$\pm 1700$

	$W_D$			$W_E$		
Bin 1	450	$\pm 640$	$\pm 410$	-250	$\pm 470$	$\pm 130$
Bin 2	500	$\pm 1200$	$\pm 300$	-1370	$\pm 810$	$\pm 530$
Bin 3	500	$\pm 3500$	$\pm 1200$	4300	$\pm 2100$	$\pm 600$
Bin 4	3300	$\pm 5800$	$\pm 1600$	-40	$\pm 3600$	$\pm 700$
Bin 5	4000	$\pm 1800$	$\pm 600$	-500	$\pm 720$	$\pm 180$
Bin 6	7500	$\pm 4200$	$\pm 900$	-4100	$\pm 2000$	$\pm 400$
Bin 7	1100	$\pm 5600$	$\pm 2600$	300	$\pm 2800$	$\pm 600$
Bin 8	1400	$\pm 3000$	$\pm 1200$	1300	$\pm 1600$	$\pm 400$
Bin 9	2700	$\pm 3100$	$\pm 900$	1500	$\pm 1300$	$\pm 600$
Bin 10	6700	$\pm 5000$	$\pm 1500$	1200	$\pm 2200$	$\pm 700$
Bin 11	6100	$\pm 3600$	$\pm 1400$	-4000	$\pm 1900$	$\pm 1000$
Bin 12	5000	$\pm 13000$	$\pm 2000$	-7800	$\pm 5900$	$\pm 1800$
Bin 13	3000	$\pm 1900$	$\pm 600$	30	$\pm 760$	$\pm 280$
Bin 14	1400	$\pm 2500$	$\pm 1300$	-3500	$\pm 900$	$\pm 1300$
Bin 15	5800	$\pm 3800$	$\pm 1400$	-200	$\pm 1100$	$\pm 500$
Bin 16	-9400	$\pm 8000$	$\pm 2800$	-4200	$\pm 2500$	$\pm 700$
Bin 17	1600	$\pm 1500$	$\pm 200$	-30	$\pm 430$	$\pm 80$
Bin 18	10100	$\pm 6100$	$\pm 3100$	-2100	$\pm 1800$	$\pm 300$
Bin 19	4900	$\pm 4800$	$\pm 1500$	-1300	$\pm 1100$	$\pm 500$
Bin 20	1500	$\pm 1700$	$\pm 500$	20	$\pm 320$	$\pm 90$
Bin 21	-1700	$\pm 3500$	$\pm 700$	10	$\pm 710$	$\pm 120$

Table 6: The hadronic structure functions  $W_A$ ,  $W_C$ ,  $W_D$  and  $W_E$  for each  $(Q^2, s_1, s_2)$  bin. For each structure function, the central value, statistical and systematic errors are given. The contributions shown in table 8 are included in the systematic errors.

	$W_F$			$W_H$		
Bin 1	-1600	$\pm 630$	$\pm 340$	60	$\pm 700$	$\pm 200$
Bin 2	130	$\pm 1300$	$\pm 400$	-100	$\pm 1300$	$\pm 600$
Bin 3	1300	$\pm 3200$	$\pm 1000$	-7000	$\pm 3600$	$\pm 1000$
Bin 4	-600	$\pm 7000$	$\pm 1200$	8400	$\pm 6200$	$\pm 3700$
Bin 5	30	$\pm 1900$	$\pm 700$	-400	$\pm 1600$	$\pm 500$
Bin 6	-5600	$\pm 4100$	$\pm 1100$	-5300	$\pm 4300$	$\pm 1800$
Bin 7	4300	$\pm 5600$	$\pm 1100$	1000	$\pm 6000$	$\pm 1200$
Bin 8	-4900	$\pm 3200$	$\pm 1200$	-5900	$\pm 3000$	$\pm 1700$
Bin 9	-2000	$\pm 2900$	$\pm 1600$	100	$\pm 3100$	$\pm 700$
Bin 10	3500	$\pm 5700$	$\pm 1000$	6700	$\pm 5200$	$\pm 1100$
Bin 11	-3100	$\pm 4600$	$\pm 900$	-2800	$\pm 4800$	$\pm 700$
Bin 12	-700	$\pm 14800$	$\pm 4900$	-14000	$\pm 15000$	$\pm 4000$
Bin 13	3200	$\pm 2100$	$\pm 400$	1900	$\pm 2100$	$\pm 400$
Bin 14	800	$\pm 3100$	$\pm 1400$	-4300	$\pm 2400$	$\pm 1800$
Bin 15	1700	$\pm 3900$	$\pm 1900$	-1100	$\pm 4000$	$\pm 900$
Bin 16	7800	$\pm 8400$	$\pm 1700$	3500	$\pm 8400$	$\pm 2300$
Bin 17	-300	$\pm 1500$	$\pm 200$	2000	$\pm 1600$	$\pm 300$
Bin 18	-5000	$\pm 5700$	$\pm 1700$	3800	$\pm 7200$	$\pm 1600$
Bin 19	4000	$\pm 5100$	$\pm 1100$	-1900	$\pm 5600$	$\pm 900$
Bin 20	100	$\pm 1800$	$\pm 400$	-1500	$\pm 1800$	$\pm 1000$
Bin 21	-5400	$\pm 3800$	$\pm 1800$	10200	$\pm 4700$	$\pm 2500$

	$X_1$			$X_2$		
Bin 1	-50	$\pm 150$	$\pm 110$	-10	$\pm 150$	$\pm 130$
Bin 2	120	$\pm 280$	$\pm 130$	-80	$\pm 310$	$\pm 60$
Bin 3	1040	$\pm 810$	$\pm 540$	450	$\pm 800$	$\pm 320$
Bin 4	-1900	$\pm 1200$	$\pm 1000$	1900	$\pm 1400$	$\pm 900$
Bin 5	20	$\pm 310$	$\pm 70$	40	$\pm 350$	$\pm 80$
Bin 6	370	$\pm 870$	$\pm 460$	-160	$\pm 850$	$\pm 220$
Bin 7	-600	$\pm 1400$	$\pm 300$	100	$\pm 1300$	$\pm 300$
Bin 8	-560	$\pm 630$	$\pm 300$	380	$\pm 680$	$\pm 140$
Bin 9	-690	$\pm 610$	$\pm 240$	810	$\pm 620$	$\pm 220$
Bin 10	-800	$\pm 1100$	$\pm 200$	-3500	$\pm 1100$	$\pm 600$
Bin 11	-1330	$\pm 770$	$\pm 260$	-210	$\pm 890$	$\pm 220$
Bin 12	-3100	$\pm 2700$	$\pm 800$	1900	$\pm 3000$	$\pm 700$
Bin 13	130	$\pm 360$	$\pm 320$	-340	$\pm 380$	$\pm 70$
Bin 14	-10	$\pm 450$	$\pm 250$	-100	$\pm 530$	$\pm 310$
Bin 15	170	$\pm 650$	$\pm 200$	-100	$\pm 650$	$\pm 250$
Bin 16	2000	$\pm 1400$	$\pm 300$	-1900	$\pm 1400$	$\pm 600$
Bin 17	300	$\pm 200$	$\pm 100$	350	$\pm 230$	$\pm 50$
Bin 18	-1900	$\pm 1100$	$\pm 400$	-400	$\pm 1000$	$\pm 200$
Bin 19	-260	$\pm 780$	$\pm 460$	10	$\pm 710$	$\pm 140$
Bin 20	250	$\pm 240$	$\pm 70$	110	$\pm 240$	$\pm 80$
Bin 21	80	$\pm 520$	$\pm 90$	340	$\pm 520$	$\pm 120$

Table 7: *The hadronic structure functions  $W_F$ ,  $W_H$ ,  $X_1$ , and  $X_2$  for each  $(Q^2, s_1, s_2)$  bin. For each structure function, the central value, statistical and systematic errors are given. The contributions shown in table 8 are included in the systematic errors.*

	$\Delta W_A$	$\Delta W_C$	$\Delta W_D$	$\Delta W_E$
Efficiency	$\pm 22\%$	$\pm 7\%$	$\pm 2\%$	$\pm 3\%$
Detector resolution	$< 0.1\%$	$\pm 13\%$	$\pm 17\%$	$\pm 3\%$
Migration	$\pm 52\%$	$\pm 19\%$	$\pm 11\%$	$\pm 14\%$
Background contribution	$\pm 1\%$	$\pm 2\%$	$\pm 1\%$	$\pm 1\%$
$\tau^- \rightarrow \pi^- \pi^- \pi^+ \pi^0 \nu_\tau$ decay modelling	$\pm 23\%$	$\pm 22\%$	$\pm 30\%$	$\pm 28\%$
Kaon channels	$\pm 1\%$	$\pm 17\%$	$\pm 19\%$	$\pm 28\%$
Monte Carlo statistics	$\pm 0.5\%$	$\pm 20\%$	$\pm 20\%$	$\pm 24\%$
$P_\tau$	$< 0.1\%$	$\pm 0.1\%$	$\pm 0.1\%$	$\pm 0.1\%$
	$\Delta W_F$	$\Delta W_H$	$\Delta X_1$	$\Delta X_2$
Efficiency	$\pm 3\%$	$\pm 6\%$	$\pm 5\%$	$\pm 3\%$
Detector resolution	$\pm 20\%$	$\pm 21\%$	$\pm 5\%$	$\pm 5\%$
Migration	$\pm 9\%$	$\pm 11\%$	$\pm 13\%$	$\pm 10\%$
Background contribution	$\pm 1\%$	$\pm 1\%$	$\pm 1\%$	$\pm 1\%$
$\tau^- \rightarrow \pi^- \pi^- \pi^+ \pi^0 \nu_\tau$ decay modelling	$\pm 11\%$	$\pm 13\%$	$\pm 24\%$	$\pm 34\%$
Kaon channels	$\pm 23\%$	$\pm 21\%$	$\pm 23\%$	$\pm 21\%$
Monte Carlo statistics	$\pm 33\%$	$\pm 27\%$	$\pm 31\%$	$\pm 26\%$
$P_\tau$	$\pm 0.3\%$	$\pm 0.3\%$	$< 0.1\%$	$\pm 0.1\%$

Table 8: *Estimated contributions to the total systematic errors for the hadronic structure functions, averaged over the bins.*

	$\Delta\gamma_{VA}$	$\Delta\gamma_{VA}^{\text{KS}}$	$\Delta\gamma_{VA}^{\text{IMR}}$
Background fraction	$< 0.01$	$< 0.01$	$< 0.01$
Kaon channels	$\pm 0.06$	$\pm 0.03$	$\pm 0.05$
$\tau^- \rightarrow \pi^- \pi^- \pi^+ \pi^0 \nu_\tau$ decay modelling	$< 0.01$	$< 0.01$	$< 0.01$
Efficiency	$< 0.01$	$< 0.01$	$< 0.01$
Detector resolution	$\pm 0.09$	$\pm 0.02$	$\pm 0.03$
Migration	$\pm 0.01$	$< 0.01$	$< 0.01$
$P_\tau$	$\pm 0.03$	$\pm 0.01$	$\pm 0.02$
Variation of the model parameters	—	$\pm 0.01$	$\pm 0.12$
total systematic error	$\pm 0.11$	$\pm 0.04$	$\pm 0.14$
statistical error	$\pm 0.26$	$\pm 0.16$	$\pm 0.21$

Table 9: *Estimated error contributions for the measurements of  $\gamma_{VA}$ .  $\Delta\gamma_{VA}$  represents the model independent measurement errors, while  $\Delta\gamma_{VA}^{\text{KS}}$  and  $\Delta\gamma_{VA}^{\text{IMR}}$  represent the errors for the KS and IMR models.*

# OPAL

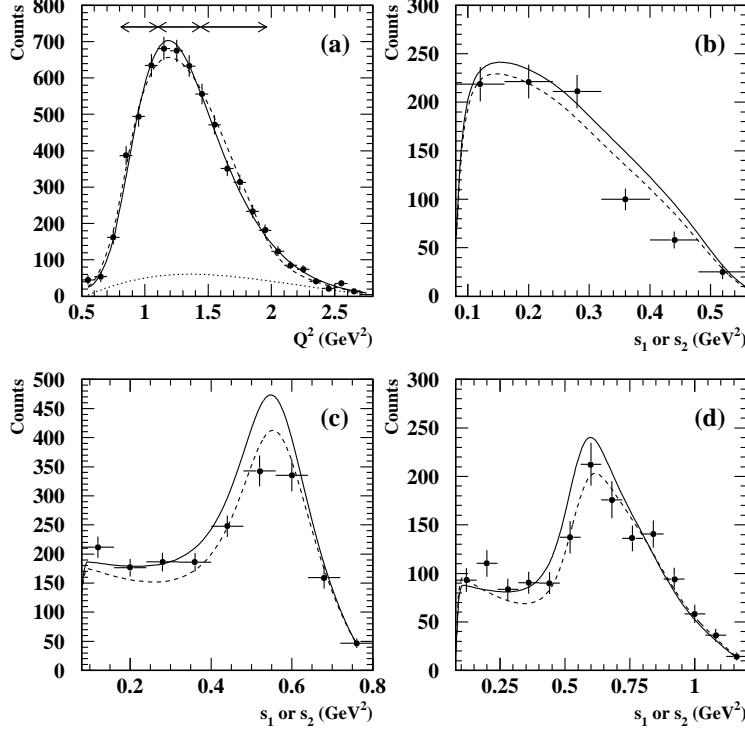


Figure 1: *The model fits of the  $3\pi$  (a) and  $2\pi$  (b, c, and d) data distributions. The data shown have been corrected for background and efficiency. The detector resolution is folded into the models. The solid line is the KS model fit and the dashed line is the IMR model fit. The dotted line under the  $3\pi$  distribution is the polynomial background contribution of the IMR model. For the KS model, the three  $2\pi$  distributions are derived using the parameters, including the normalization, from the fit to the  $3\pi$  distribution. The IMR model fit is a global fit of all four histograms. The  $Q^2$  intervals for the  $2\pi$  distributions, indicated by the arrows in (a), are (b)  $0.81 < Q^2 < 1.10 \text{ GeV}^2$ , (c)  $1.10 < Q^2 < 1.44 \text{ GeV}^2$ , and (d)  $1.44 < Q^2 < 1.96 \text{ GeV}^2$ .*



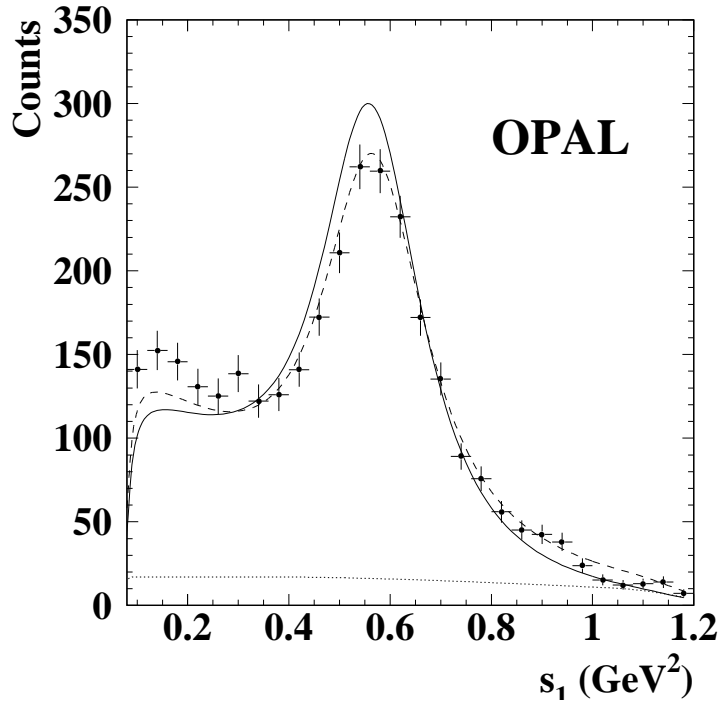


Figure 2: *The data for the uncut Dalitz-plot projection is overlaid by each of the two models. The data has been corrected for background and efficiency. The detector resolution is folded into the models. The solid line is the KS model and the dashed line is the IMR model. The  $Q^2$  dependent polynomial background term of the IMR model has been included for that model, and its contribution is shown as the dotted line.*

## OPAL

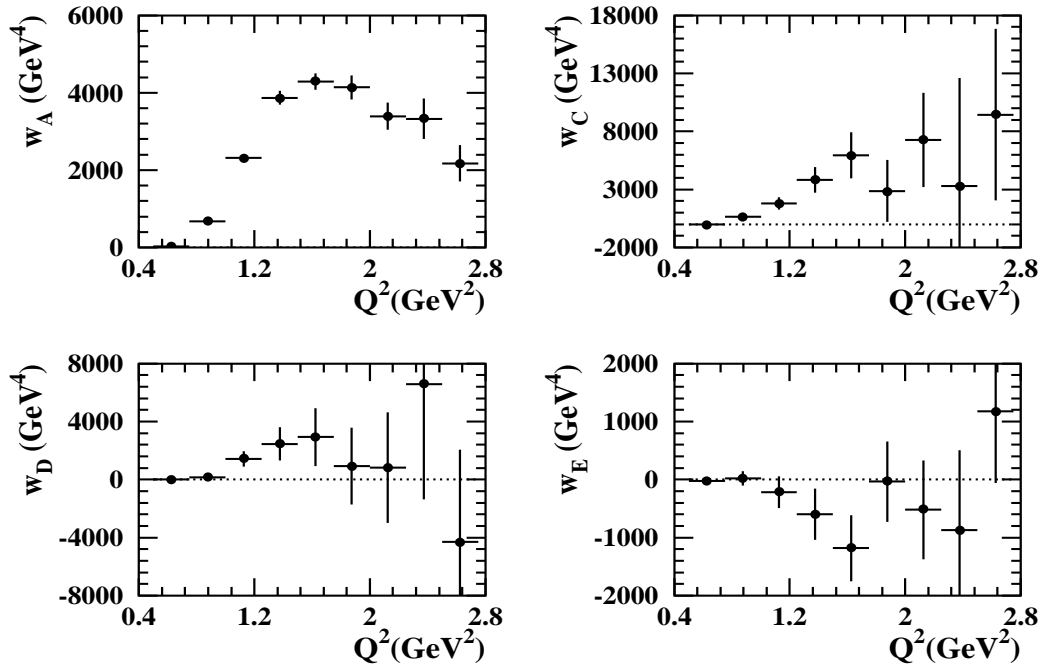


Figure 3: Measured structure functions  $w_A$ ,  $w_C$ ,  $w_D$ , and  $w_E$  as functions of  $Q^2$ . The error bars represent the statistical and systematic errors added in quadrature.

# OPAL

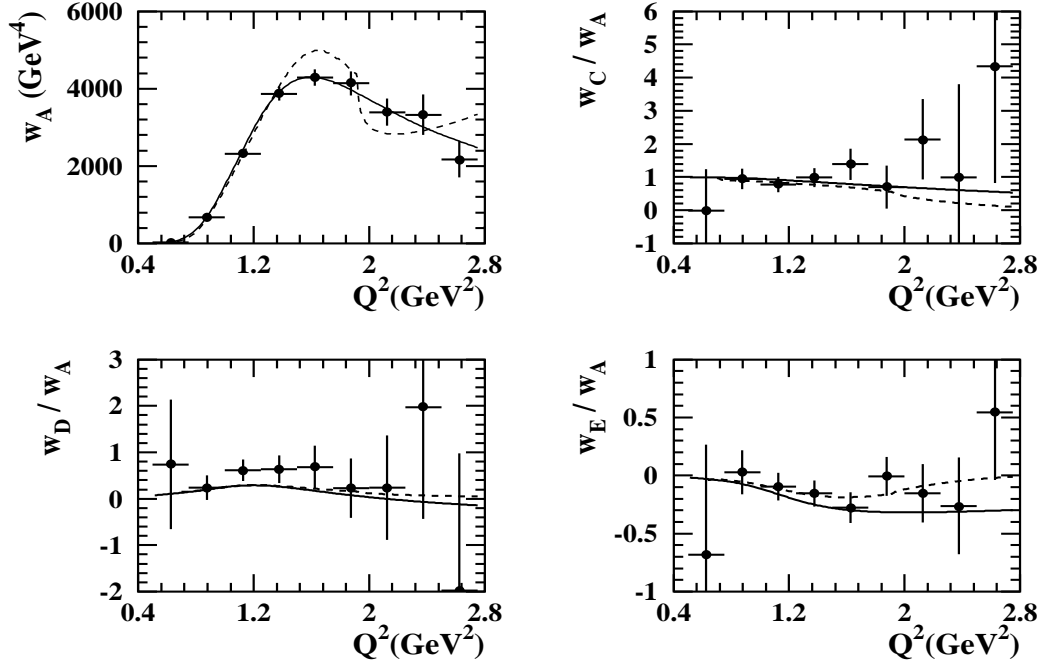


Figure 4: Comparison of the measured structure functions  $w_A$ ,  $w_C/w_A$ ,  $w_D/w_A$ , and  $w_E/w_A$  (points with error bars) with the predictions of the KS model (solid line) and the IMR model (dashed line). The IMR model prediction for  $w_A$  includes the polynomial background term. With both models there is good agreement between the model predicted and the data angular distributions for  $w_C/w_A$ ,  $w_D/w_A$ , and  $w_E/w_A$ . For the  $w_A$  distribution, however, the KS model is preferred over the IMR model.

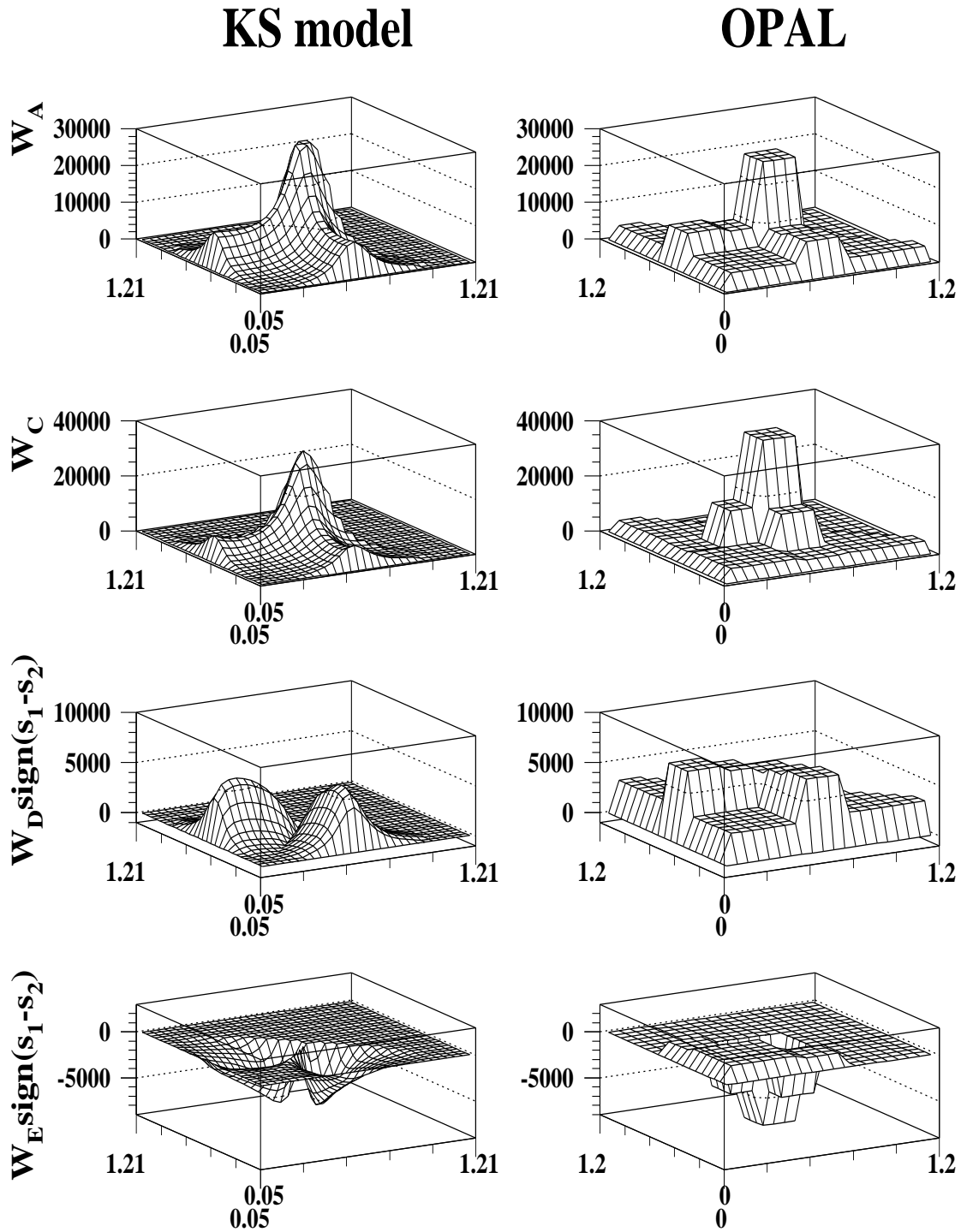


Figure 5: Qualitative comparison of the axial-vector structure functions  $W_A$ ,  $W_C$ ,  $W_D$ , and  $W_E$  between the measurement (for  $1.21\text{GeV}^2 < Q^2 < 1.44\text{GeV}^2$ ) and the KS model prediction (for  $Q^2 = 1.3\text{GeV}^2$ ) in the Dalitz plane. The fit result from the lower half of the Dalitz plane ( $s_1 > s_2$ ) is mirrored to the upper half for improved clarity. The shapes of the distributions are correctly predicted by the model.

# OPAL

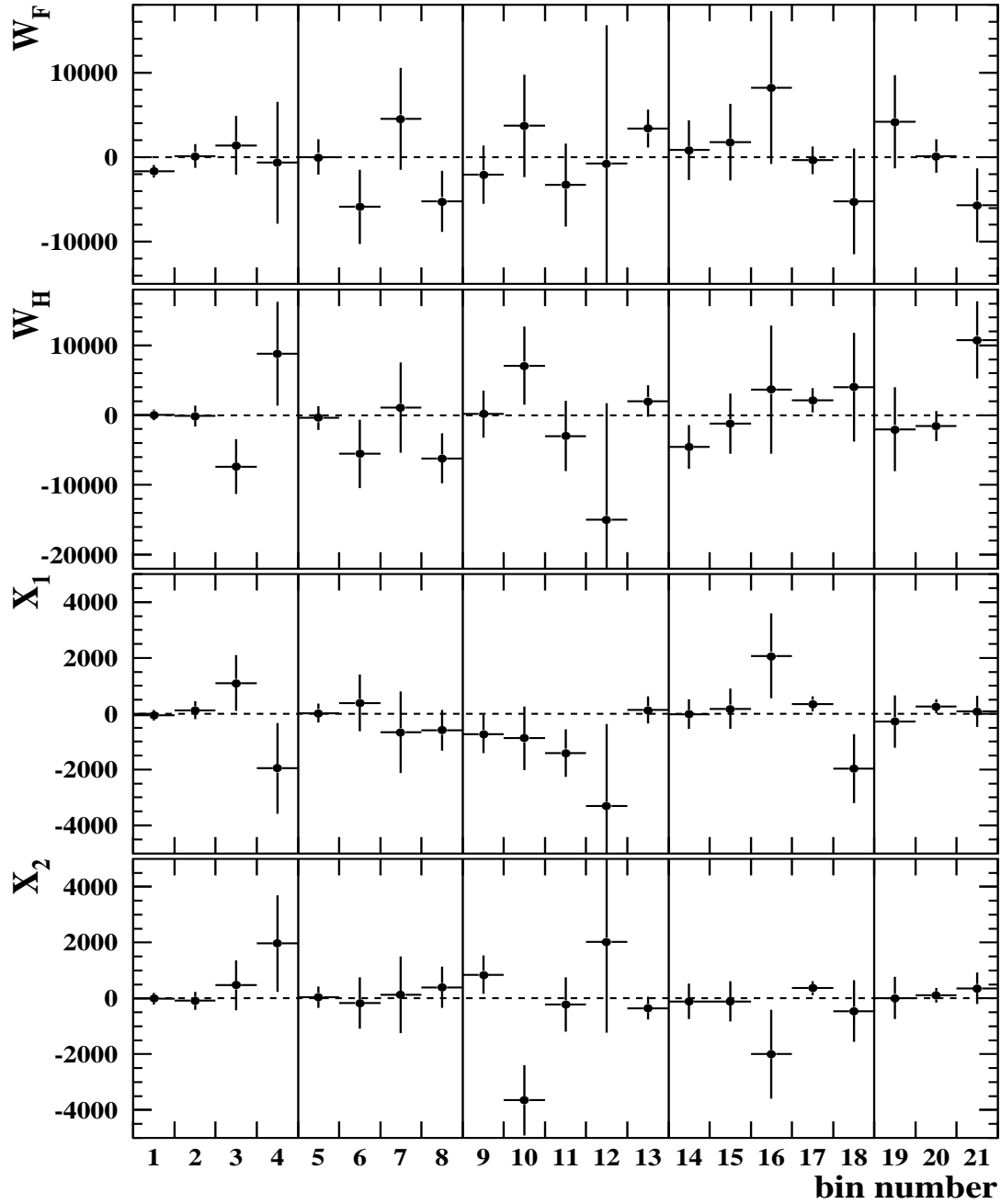


Figure 6: Comparison of the measured structure functions  $W_F$ ,  $W_H$ ,  $X_1$ , and  $X_2$  (points with error bars) with the null hypothesis for scalar and vector components for each bin. See table 4 for an explanation of the bin numbers.

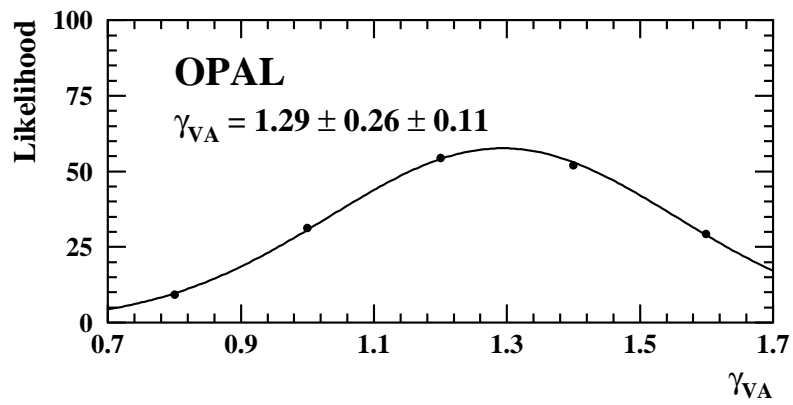


Figure 7: *The likelihood as a function of  $\gamma_{VA}$  (points), with arbitrary normalisation. The solid line is a Gaussian interpolation.*